Radial distribution and strong lensing statistics of satellite galaxies and substructure using high-resolution ΛCDM hydrodynamical simulations

Andrea V. Macciò,[1]⋆ Ben Moore,[1] Joachim Stadel[1] and Jürg Diemand[1,2]

[1]*Institute for Theoretical Physics, University of Zürich, Winterthurerstrasse 190, CH-8057 Zürich, Switzerland*
[2]*Department of Astronomy & Astrophysics, University of California, 1150 High Street, Santa Cruz, CA 95064, USA*

ABSTRACT

We analyse the number density and radial distribution of substructures and satellite galaxies using cosmological simulations that follow the gas dynamics of a baryonic component, including shock heating, radiative cooling and star formation within the hierarchical concordance Lambda cold dark matter model. We find that the dissipation of the baryons greatly enhances the survival of subhaloes, especially in the galaxy core, resulting in a radial distribution of satellite galaxies that closely follows the overall mass distribution. Hydrodynamical simulations are necessary to resolve the adiabatic contraction and dense cores of galaxies, resulting in a total number of satellites a factor of 2 larger than that found in pure dark matter simulation, in good agreement with the observed spatial distribution of satellite galaxies within galaxies and clusters. Convergence tests show that the cored distribution found by previous authors in pure *N*-body simulations was due to the physical overmerging of dark matter only structures.

We proceed to use a ray-shooting technique in order to study the impact of these additional substructures on the number of violations of the cusp caustic magnification relation. We develop a new approach to try to disentangle the effect of substructures from the intrinsic discreteness of *N*-body simulations. Even with the increased number of substructures in the centres of galaxies, we are not able to reproduce the observed high numbers of discrepancies observed in the flux ratios of multiply lensed quasars.

Key words: gravitational lensing – methods: numerical – galaxies: clusters: general – galaxies: haloes – cosmology: theory – dark matter.

1 INTRODUCTION

The study of substructures within simulated galaxy-sized haloes has posed interesting problems to the current, widely accepted, Lambda cold dark matter (ΛCDM) scenario. As pointed out previously (Klypin et al. 1999; Moore et al. 1999), the number of surviving subhaloes found in *N*-body simulations greatly exceeds the number of observed satellites around the Milky Way and Andromeda. The properties of subhaloes on different scales have been the subject of many recent studies which have pushed the resolution of dissipationless simulations (Ghigna et al. 1998, 2000; Moore et al. 1998; Colin, Klypin & Kravtsov 2000; De Lucia et al. 2004; Diemand, Moore & Stadel 2004; Gao et al. 2004a; Kravtsov, Gnedin & Klypin 2004; Reed et al. 2005; Zentner et al. 2005a,b). The kinematical properties of subhaloes are now well understood – they make up a fraction between 5 and 10 per cent of the mass of virialized haloes on scales relevant to observational cosmology.

Most of these previous studies used dissipationless cosmological simulations; although non-baryonic dark matter exceeds baryonic matter by a factor of $\Omega_{\mathrm{dm}}/\Omega_{\mathrm{b}} \simeq 6$ on average, the gravitational field in the central region of galaxies is dominated by stars and gas. In the hierarchical galaxy formation model, stars are formed by the condensation of cooling baryons at the halo centre. The cooling baryons increase the density in the central halo region mainly not only because of the extra mass associated with the inflow but also because of the adiabatic contraction of the total mass distribution (Blumenthal et al. 1986; Loeb & Peebles 2003; Gao et al. 2004b; Gnedin et al. 2004). This process acts *both* for the host halo and for its subhaloes, therefore we may expect that the dark matter substructure haloes formed within hydrodynamical simulations will experience a different tidal force field and they themselves will be more robust to tidal effects. Since overmerging of dark matter substructures is sensitive to their central structure (Moore, Katz & Lake 1996), pure *N*-body simulations may bias results because of physical overmerging (Diemand et al. 2004, DMS04 hereafter).

The fact that substructure haloes are spatially more extended than the averaged mass distribution was first pointed out by Ghigna et al. (1998). By increasing the resolution by over an order of mag-

⋆E-mail: andrea@physik.unizh.ch

nitude, DMS04 showed that this result was independent of the numerical resolution. Furthermore, the distribution of galaxies in clusters appears to follow the overall mass distribution, quite unlike the subhaloes selected by the final bound mass in pure dark matter simulations. By tracing haloes backwards and forwards in time through the simulations, they argued that the missing central subhaloes may be destroyed by tidal forces at redshifts higher than $z = 5$. The survival of substructure and galaxies within dense environments has implications for indirect detection techniques, for example using image distortions of gravitationally lensed distant quasars by foreground galaxies and their dark matter haloes.

It has been argued that a possible signature of the presence of dark matter substructures can be found in strong gravitational lensing of quasi-stellar objects (QSOs) (Mao & Schneider 1998; Metcalf & Madau 2001; Chiba 2002; Metcalf & Zhao 2002; Chen, Kravtsov & Keeton 2003; Amara et al. 2004; Dalal & Kochanek 2002; Kochanek & Dalal 2004; Mao et al. 2004). If a distant image source is close to (or inside) a cusp in a caustic curve, three of the images will be clustered together and the sum of their magnifications will be zero (Zakharov 1995), taking the negative parity image to have negative magnification. This relation holds for a wide class of smooth analytic lens models (i.e. Schneider & Weiss 1992; Keeton, Gaudi & Petters 2003); on the other hand, all known observed lensed QSOs violate this relation which has been explained as due to the presence of the CDM substructure within the lensing galaxy's halo. However, some of these discrepant systems may be due to microlensed stars rather than due to the CDM substructure (Keeton et al. 2003). Bradač et al. (2004) analysed a low-resolution simulation of a galaxy and claim that the level of substructure present in simulations produces violations of the cusp relation comparable to those observed. Amara et al. (2004) implanted an idealized model of galaxy into the centre of a high-resolution galactic halo extracted from dissipationless *N*-body simulations to test the effects of substructure on lensed images. Their findings contrast those of Bradač et al. (2004) since they found that the substructures produced in a ΛCDM halo are not abundant enough to account for the cusp caustic violation observed, these results are also confirmed by Mao et al. (2004), based on the analysis of substructure abundance in pure dark matter simulations.

The first part of this paper is devoted to the analysis of the subhalo population around a galaxy-sized halo that forms in a large cosmological simulation simulated with dark matter only and then with the inclusion of a baryonic component. In Section 2, we present the numerical simulations, our halo-finding scheme and resolution tests. The properties of the main halo and its satellites are presented in Section 3. Comparison with observations and a discussion of the results are presented in Section 4. In the second part of this paper, we re-examine the effects of substructures on multiply lensed quasar images using our new hydrodynamic galaxy simulation in combination with a ray-shooting technique. In Section 5.1, we present the lensing code, while Section 5.2 is devoted to multiple images analysis. In Sections 6 and 7, we present our results and the conclusions of our work.

2 NUMERICAL SIMULATIONS

The simulations were performed with GASOLINE, a multistepping, parallel TreeSPH *N*-body code (Stadel 2001; Wadsley, Stadel & Quinn 2004). We include radiative and Compton cooling for a primordial mixture of hydrogen and helium. The star formation algorithm is based on the Jeans instability criteria (Katz 1992), where gas particles in dense, unstable regions and in convergent flows spawn star particles at a rate proportional to the local dynamical time (see

also Governato et al. 2004). The star formation efficiency was set to 0.1, but in the adopted scheme its precise value has only a minor effect on the star formation rate (SFR) (Katz 1992). The code also includes the supernova feedback as described by Katz (1992) and the ultraviolet (UV) background following Haardt & Madau (1996).

We have selected a candidate Galactic mass halo ($M_{dm} \approx 10^{12} M_\odot$) from an existing low-resolution dark matter only simulation in a concordance ($\Lambda = 0.7, \Omega_0 = 0.3, \sigma_8 = 0.9$) cosmology and resimulated it at higher resolution using the volume renormalization technique (Katz & White 1993), and including a gaseous component within the entire high-resolution region. The mass per particle of the dark matter and gaseous particles are, respectively, $m_d = 1.66 \times 10^6 M_\odot$ and $m_g = 3.28 \times 10^5 M_\odot$. The dark matter has a spline gravitational softening length of 200 pc, and we have about 1×10^6 particles for each component (dark and gas) in the high-resolution region.

The smoothed particle hydrodynamics (SPH) simulations with cooling are computationally expensive, and we are forced to stop the full calculation once the galaxy has formed, at a redshift $z = 1.5$. (The parallel calculation is dominated by the few remaining gas particles which need extremely small time-steps in order to satisfy the Courant criterion). In order to study the dynamical evolution of the stellar and dark matter satellites, we have evolved the simulation to the present epoch without following the remaining gaseous particles – we turn them into collisionless particles and treat only their gravitational interactions. We do not believe that this influences any of our conclusions since (i) most of the gas has already turned into stars between a redshift $z = 5.5$ and $z = 2.5$ and (ii) continuing to include cooling of the remaining gas would only allow us to resolve higher density gas clouds. Inside the virial radius at a redshift $z = 0$, we have 8.6×10^5 dark matter particles and 2.4×10^5 star particles. In Fig. 1, we show the SFR in our simulation which is in good agreement with previous numerical studies (i.e. Governato et al. 2004).

The same object has also been simulated with dark matter only using the same spatial and mass resolution as the hydro run, in addition one simulation with four times better mass resolution (this object is Gal1 in DMS04). In the following, we will refer to the three simulations as *hydro*, *dm* and *dm*HR, respectively.
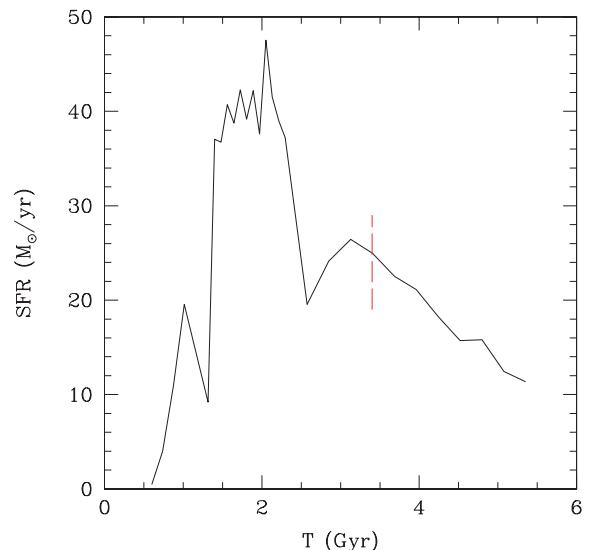

Figure 1. The SFR in the hydro simulation. The time since the big bang is indicated and the red vertical line corresponds to $z = 2$, where cooling was switched off.
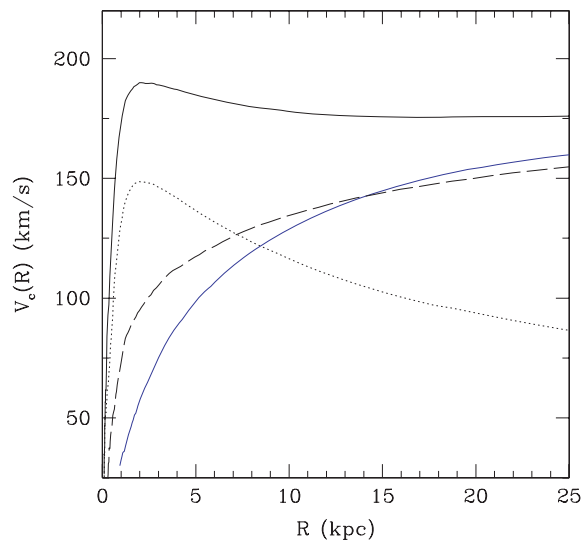
Figure 2. Rotation curve [defined as $V_c(R) = \sqrt{GM(< R)/R}$] for all components (upper solid line), star (dotted line) and dark matter (dashed line) for the galaxy at $z = 0$. For comparison, the dark matter rotation curve (lower solid line) obtained in the pure dark matter simulation of the same object is also shown.

3 HALOES PROPERTIES

3.1 Host halo

In Fig. 2, we show the rotation curve [defined as $V_c(r) = \sqrt{GM(< r)/r}$] for all components, stars and dark matter separately for the galaxy at $z = 0$. For comparison, we also show the dark matter rotation curve obtained in the pure dark matter simulation of the same object. The baryons dominate within the inner 10 kpc, and the effect of the adiabatic contraction on the dark matter can clearly be seen – the baryons have increased the mass within 5 kpc by a factor of 4. The steeper central cusp can clearly be seen in the density profile plot (Fig. 3), the *dm* halo has a profile that can be well fitted by an Navarro, Frenk & White (1996; NFW) profile with a concentration $c_{vir} = 9.6$ (defined with respect to the virial radius); on the other hand, in the presence of gas and stars the density profile in the inner region has an almost constant cusp slope $\alpha \approx -2.0$, as predicted by the adiabatic contraction model (Blumenthal et al. 1986). In Fig. 1, we show the SFR, the bulge of the galaxy forms through a series of rapid major merger events that end around $z = 2.8$, turning mostly low angular momentum gas into stars. There are no more merging events in the formation of our galaxy after $z = 2$, so even if we cannot follow the SFR directly beyond $z = 1.5$, we do not expect it to be different from a slowly decreasing function of time.

3.2 Subhaloes

Within the virial radius of the high-resolution CDM simulations, we can resolve several hundreds of substructure haloes (bound over-dense clusters of particles). We identify subhaloes with SKID (Stadel 2001), which calculates local densities using a SPH kernel, then moves particles along the density gradient until they oscillate around a point (i.e. move less than some length l). Then, they are linked together using friends-of-friends (FoF) with this l as a linking length.

SKID with $l = 4\epsilon_0$ (where ϵ_0 is the gravitational softening of the simulation) adequately identifies the smallest subhaloes and the centres of the largest subhaloes. For the latter, the calculated bound
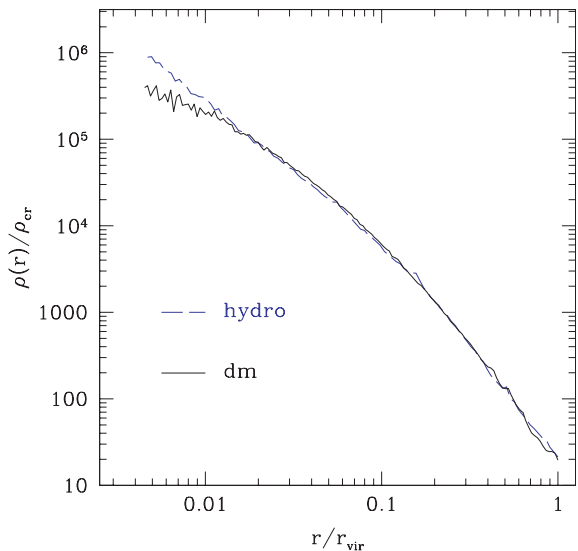

Figure 3. The dark matter density profile in the *N*-body (dashed curve) and hydro (solid line) simulations. The effect of the adiabatic contraction can clearly be seen in the inner part of the profile.

mass is underestimated. Using $l = 10\epsilon_0$ can cure this, but then some of the small subhaloes are missed. Therefore, we have used a combination of the subhalo catalogues obtained with these two linking lengths in order to create the complete catalogue of subhaloes and to calculate their correct structural parameters. We included in our study only haloes with $M > 2 \times 10^8 \, M_\odot$ (i.e. $n_{dm} > 100$).

In Fig. 4, where we plot the dark matter subhaloes mass function in the *hydro* and *dm* simulations, calculated within a sphere of radius 1 Mpc centred on the galaxy. As expected, we do not observed a big difference between the two simulations in such a large volume, this is because the presence of baryons is thought to be much more important in the inner region of our galaxy, where the tidal field is much more efficient in destroying subhaloes. The effect of baryons can easily be seen in Fig. 5, where we plot the ratio of the number of subhaloes in the two simulations as a function of the distance from
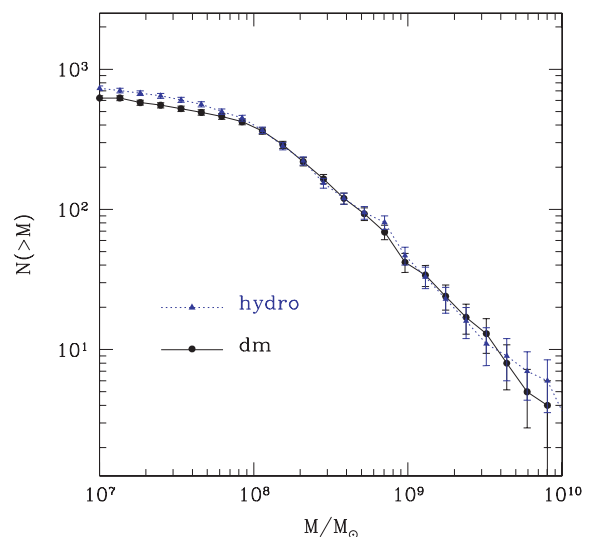

Figure 4. The dark matter subhaloes mass function in the *hydro* (black) and *dm* (blue) simulations. In a sphere of 1 Mpc around the centre of the galaxy.
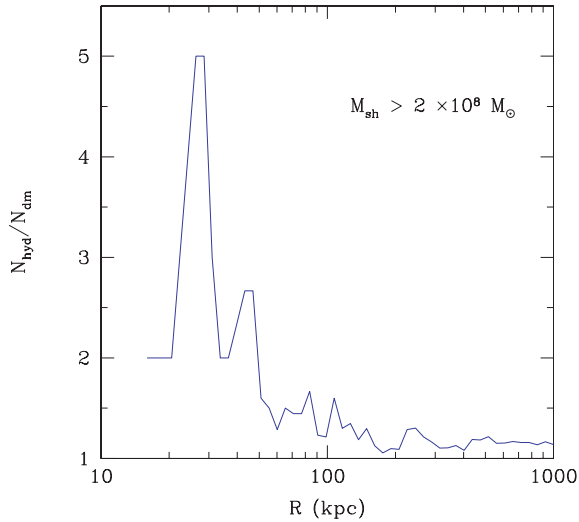
Figure 5. Ratio of the number of DM subhaloes with $M > 2 \times 10^8 \, \mathrm{M_\odot}$ in the *hydro* and *dm* runs as a function of the distance from the centre of the main halo.

Figure 6. Substructure radial density profiles for different simulations.

the centre of the galaxy. At 70 kpc ($\approx 1/3 R_{200}$), we see an increase by a factor of 2 in the numbers of surviving satellites. Within the inner 40 kpc, the number of satellites with mass greater than $2 \times 10^8 \, \mathrm{M_\odot}$ is enhanced by a factor of 4–5 over that found in the pure dark matter simulation. We found that this difference is more striking for the most massive subhaloes, the number of satellites with mass greater than $10^7 \, \mathrm{M_\odot}$ does not differ so much from the *N*-body result. This may be revealing the limitation of our resolution – the smallest haloes of mass $\sim 10^7 \, \mathrm{M_\odot}$ are just resolved with about 10 dark matter (DM) particles and are more easily destroyed through numerical effects. Another explanation could be the inhibition of star formation in smaller haloes because of the UV background and the supernovae (SN) feedback that raise the temperature of the gas and stop its collapse in the DM halo if it is not sufficiently bound (i.e. its potential well is not deep enough). Without stars, the DM can more easily be destroyed by the tidal forces of the main halo (see also Section 4, for more details on the feedback effects).

As noted by previous authors (DMS04, for a recent analysis), the spatial distribution of subhaloes in CDM simulations of galaxies is antibiased with respect to the mass; Nagai & Kravtsov (2005) have recently shown that part of this bias is due to the varying amount of mass loss at different radii, and that it is considerably smaller if instead of using the mass of satellites at $z = 0$, one uses the mass measured at the accretion time. For our purposes, we have decide to use the mass at the present time because we are interested in the different tidal forces and mass loss between the *hydro* and *dm* run.

Fig. 6 shows the relative number density of surviving satellites $M > 2 \times 10^8$ at $z = 0$, in several pure dark matter simulations and our hydro simulation. In all *dm* cases, the satellites are more extended than the overall mass distribution (dominated by the smooth dark matter background). This effect becomes larger inside of half the virial radius. Within this region, the dark matter only simulations reveal a much flatter number density distribution. The satellite distribution in the hydro simulation is much steeper and it is rather similar to the smooth mass distribution. The core distribution found in the *dm* run almost disappears, and the satellite profiles are well fitted by an NFW-like function even if they are still less concentrated than the overall mass distribution (in agreement with findings from hydro simulations on cluster scales by Nagai & Kravtsov 2005);
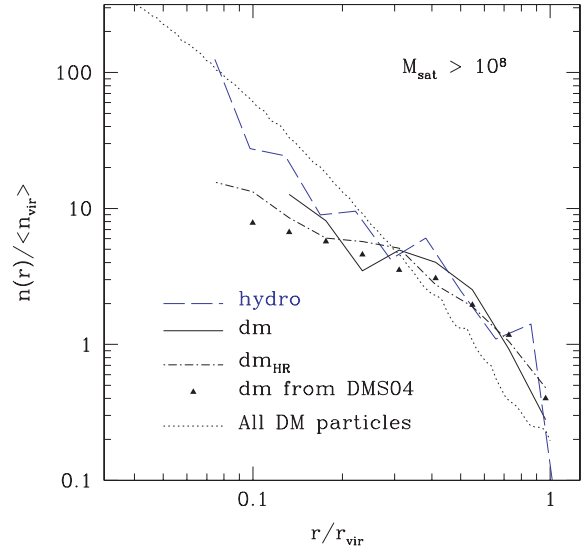
the concentration parameter (r_c/r_{vir}) for the satellite distribution is ≈ 6.5, where the one for the smooth DM distribution in the range $0.07 < r/r_{vir} < 1.0$ is $c_{DM} = 9.6$.

3.3 Resolution tests

In the hydro simulation, we have a higher mass resolution due to the presence of baryons; the mass of the star and gas particles is roughly 20 per cent of the mass of the DM particles, this means that in principle the lower number of subhaloes close to the centre that we found in the *N*-body simulation can partially be due to an over-merging phenomenon that depends on the resolution. In the lower panel of Fig. 7, we compare the number of subhaloes as a function
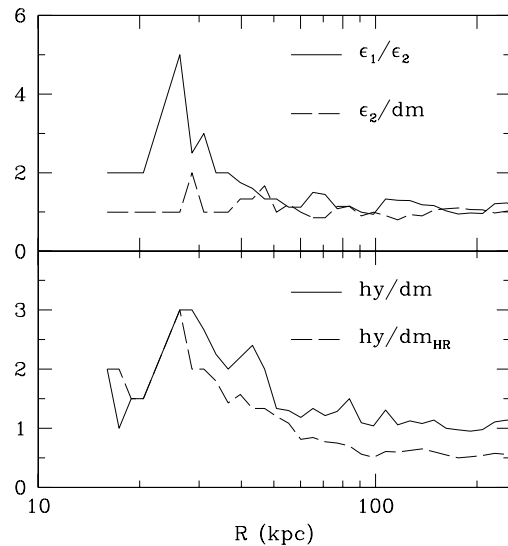

Figure 7. The effect of resolution on the number of subhaloes. Upper panel: ratio between the number of DM subhaloes ($M > 2 \times 10^8 \, \mathrm{M_\odot}$) in the hydro run for two different values of the star particles softening: $\epsilon_1 = 0.2$ kpc and $\epsilon_2 = 1.5$ kpc as a function of distance from the centre. The dashed line is the same quantity, but for the hydro run with $\epsilon = \epsilon_2$ and the *dm* run. Lower panel: the ratio between the number of DM subhaloes ($M > 10^7 \, \mathrm{M_\odot}$) in the hydro run and in the high-resolution dm_{HR} (dashed line) and low-resolution *dm* (solid line) runs.

of radius between the hydro simulation and the highest-resolution dark matter only run (dm_{HR}) which has a mass resolution of a factor of 4 better than the low-resolution case. Fig. 7 demonstrates that the increase in the number of substructure haloes in the hydro run is apparent even when compared to the higher resolution *N*-body simulation.

The second test that we have performed is related to the force resolution (gravitational softening) adopted for the star particles. Stars are concentrated in the inner few kpc of the galaxy and a small softening must be chosen to correctly follow the dynamical evolution of such high-density regions. We have run the hydro simulation for two different values of the star gravitational softening (ϵ): $\epsilon_1 = 0.2$ kpc and $\epsilon_2 = 1.5$ kpc. Results are presented in the upper panel of Fig. 7, where we show the difference in the number of subhaloes as a function of the distance from the centre. The effect of softening is important – too large a value leads to tidal disruption of satellite galaxies since they have artificially shallow central potentials and are hence less bound. The larger stellar softening ($\epsilon_2 = 1.5$ kpc) erases the stabilizing effect of the stars inside the satellites, and the radial distribution of surviving subhaloes is identical to the pure dark matter case (see the dashed line in the upper panel of Fig. 7).

4 COMPARISON WITH OBSERVATIONS

For this comparison, we used the data for the Local Group as compiled by Mateo (1998). In this sample, only relatively massive satellites with an estimated rotational velocity or a three-dimensional velocity dispersion of stars greater than 10 km s^{-1} are considered. In order to simplify the comparison even further, as in Klypin et al. (1999), we have considered the number of satellites within a radius of 280 kpc from the Milky Way and Andromeda, which is close to the expected virial radius of these galaxies.

Even though the remaining gas particles are turned into collisionless tracers at $z = 1.5$, this does not affect the kinematical properties of the satellites at $z = 0$. All of the satellites that end up within the virial radius of the galaxy halo have formed prior to this epoch. Subsequent loss of the remaining gas particles to stars or by stripping processes would not lead to significant changes to the satellite structural parameters.

In Fig. 8, we show the cumulative velocity distribution function (VDF) of satellites; the number of satellites per unit volume and per central object with internal circular velocity is larger than the given value V_c. We show the VDF for different runs: the solid line represents the results for the *dm* simulation; as already known, the CDM models overpredict the number of satellites for $V_c < 30$ km s^{-1}. The dashed line represents the results from Klypin et al. (1999), that were originally compared with the data from Mateo (1998). The simulation results agree quite well above 20 km s^{-1}; our higher resolution pure dark matter simulations allow us to follow the distribution of subhaloes to lower circular velocities ($V_c > 10$ km s^{-1}).

The open circles connected by a solid line show the VDF of dark matter haloes for the hydro run. The number of satellites in the range $15 < V_c < 30$ km s^{-1} is increased, and now also for $V_c > 35$ km s^{-1} there is an over abundance of satellites. We have also computed the VDF for satellites in the hydro run considering only their stars, shown by squares connected with the long dashed line. This is a fairer comparison since we are comparing stellar kinematics in each case. Stars are more concentrated than the DM, so they trace the dynamics within a smaller central region; this explains why the VDF for stars is below the DM one over the whole velocity range (Hayashi et al. 2004), but this effect is too small to reconcile the simulations with the observations of Local Group satellites.
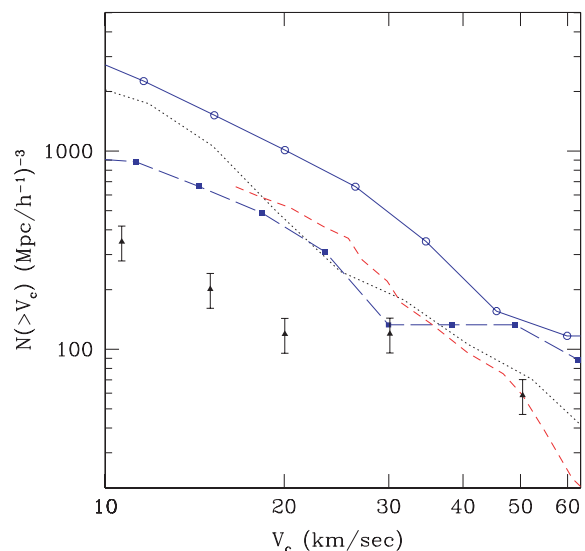

Figure 8. The cumulative circular VDF of satellites. The black dotted line represents the results for the DM-only simulation, the blue dashed line is the VDF for stars (visible) haloes and the solid blue line is for DM haloes. Black triangles with error bars show average results for Milky Way and Andromeda satellites (Mateo 1998; Klypin et al. 1999). The red dashed line is the result for a ΛCDM dissipationless galaxy obtained by Klypin et al. (1999).
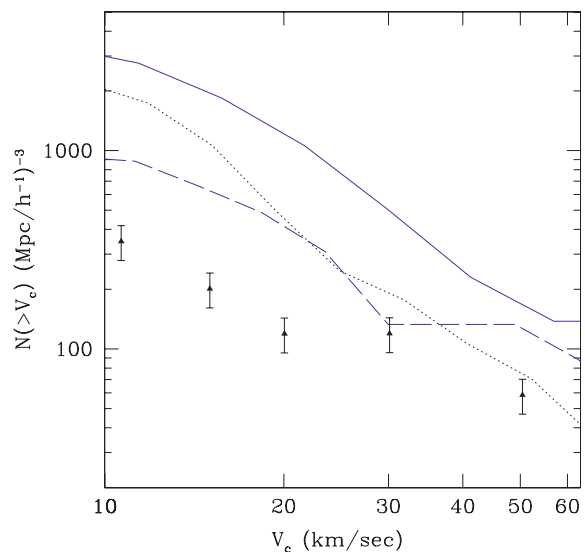

Figure 9. Similar to Fig. 8. The solid (blue) line is the stellar satellite VDF in the absence of the SN feedback, the dashed line is the feedback turned on and black dotted line represents the results for the DM only simulation.

Another clear difference between the two VDFs is that we have no stellar satellites with $V_c < 15$ km s^{-1}, which is due to the SN feedback and the UV background in the simulation. To confirm this, we have run a full hydrodynamical simulation without these external feedback sources, shown in Fig. 9, where the VDF for the no feedback case continues to rise within $V_c < 15$. With the weak feedback used in this paper, hydrodynamic cosmological simulations produce VDFs which lie above the pure dark matter results and the discrepancy to Local Group observations becomes even larger. Runs with the strong feedback from reionization are able to produce realistic

VDFs, we will present such runs in a forthcoming paper (Macciò et al. , in preparation).

5 LENSING ANALYSIS

Quasars that are being gravitationally lensed into multiple images have recently been used to place limits on the surface density of CDM subhaloes (Mao & Schneider 1998; Metcalf & Madau 2001; Chiba 2002; Dalal & Kochanek 2002; Metcalf & Zhao 2002; Chen et al. 2003; Amara et al. 2004; Bradač et al. 2004; Mao et al. 2004). Small mass clumps that happen to lie near the images affect the observed magnification ratios. The question arises as to whether these observations are compatible with distortions expected to occur from dark matter substructures and satellite galaxies within the ΛCDM model. In the following, we will first present our lensing code, then we will briefly recall the main features of the so-called cusp relation, and finally we will report our results.

5.1 Lensing simulations

Our ray-shooting code is described in detail in Macciò (2005); here we will only summarize its main features. The galaxy is centred in a cube of length 0.6 Mpc and we study three lens images, obtained by projecting the particle positions along the three coordinate axes. We then divide the projected density field, Σ, by the critical surface mass density for lensing

$$\Sigma_{cr} = \frac{c^2}{4\pi G} \frac{D_S}{D_L D_{LS}}, \tag{1}$$

thus obtaining the convergence k. Here, c is the speed of light, G is the gravitational constant, while D_L, D_S, D_{LS} are the angular-diameter distances between lens and observer, source and observer, lens and source, respectively. In the following, we adopt $z_L = 0.3$ for the lens redshift and $z_s = 3.0$ for the source redshift.

The deflection angle due to this 2D particle distribution, on a given point x on the lens plane reads

$$\boldsymbol{\alpha}(\boldsymbol{x}) = \sum_{j=1}^{N} \frac{4G}{c^2} \frac{m_j}{|\boldsymbol{x} - \boldsymbol{y}_j|}. \tag{2}$$

Here, $\boldsymbol{y}_j$ is the position of the jth particle and N is the total number of particles.

Since a direct summation requires a long time, we speed up the code by using a P^{3}M-like algorithm; the lens plane was divided into 256×256 cells and the direct summation was applied to particles belonging to the same cell of x and for its eight neighbour cells. Particles in other cells were then seen as a single particle in the cell barycentre, given the total mass of the particles inside the cell. The deflection angle diverges when the distance between a light ray and a particle is zero. To avoid this unwanted feature, we introduce a softening parameter, ϵ, in equation (2); the value ϵ is tuned to the resolution of the current simulation.

We start to compute $\boldsymbol{\alpha}(\boldsymbol{x})$ on a regular grid of 4096×4096 test rays that cover the central quarter of the lens plane (multiple images form very close to the lens centre). This resolution does not provide enough pixels in the inner regions affected by strong lensing to model lensing properties in the correct way. The resolution is increased by extracting the central region, where strong lensing is occurring and using bilinear interpolation to calculate the relevant quantities to higher resolution. Our final resolution is equivalent to a bundle of $16\,384 \times 16\,384$ light rays.

The relation between image and sources positions is given by the lens equation

$$\boldsymbol{y} = \boldsymbol{x} - \boldsymbol{\alpha}(\boldsymbol{x}); \tag{3}$$

the local properties of the lens mapping are then described by the Jacobian matrix of the lens equation

$$A_{hk}(\boldsymbol{x}) = \frac{\partial y_h}{\partial x_k} = \delta_{hk} - \frac{\partial \alpha_h}{\partial x_k}, \tag{4}$$

and the magnification factor μ is given by the Jacobian determinant of A:

$$\mu(\boldsymbol{x}) = \frac{1}{\det A} = [A_{11}(\boldsymbol{x})A_{22}(\boldsymbol{x}) - A_{12}(\boldsymbol{x})A_{21}(\boldsymbol{x})]^{-1}. \tag{5}$$

Finally, the Jacobian also determines the location of the critical curves $\boldsymbol{x}_c$ on the lens plane, which are defined by $\det A(\boldsymbol{x}_c) = 0$. Because of the finite grid resolution, we can only approximately locate them by looking for pairs of adjacent cells with opposite signs of $\det A$. Then, the lens equations

$$\boldsymbol{y}_c = \boldsymbol{x}_c - \boldsymbol{\alpha}(\boldsymbol{x}_c), \tag{6}$$

yield the corresponding caustics $\boldsymbol{y}_c$, on the source plane.

To find the images of an extended source, all image-plane positions x are checked to see if the corresponding entry in the map table $\boldsymbol{y}$ lies within the source, i.e. for a circular source with radius r_c and centred in $(y_1^c; y_2^c)$, it is checked if

$$\left(y_1 - y_1^c\right)^2 + \left(y_2 - y_2^c\right)^2 \leqslant r_c^2, \tag{7}$$

where (y_1, y_2) is the component of the vector $\boldsymbol{y}$. The sources are modelled as circles with a radius of 60 pc according to Amara et al. (2004). Those points fulfilling the previous equation are a part of one of the source images and are called image points. We then use the standard FoF algorithm to group together image points within connected regions since they belong to the same image.

A typical lens configuration is shown in Fig. 10, where critical lines, caustic lines, source and images positions are indicated. The images within the black circles correspond to those selected for the cusp relation investigation.
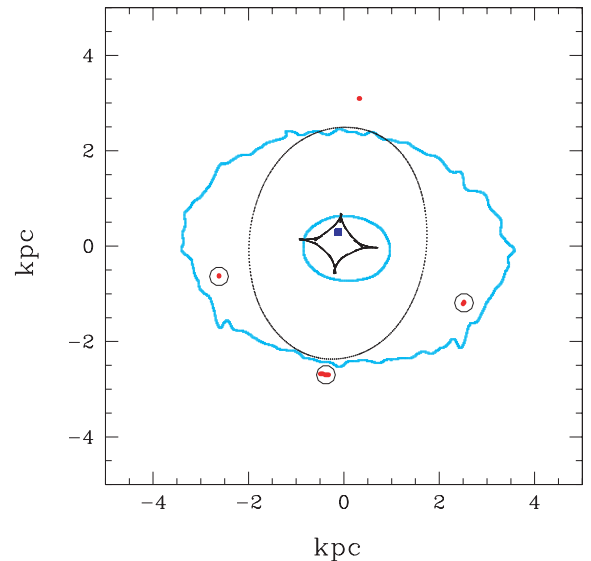

Figure 10. Basic lens configuration. The caustic surface is shown as a black line, and critical curves are shown as cyan lines. The four images that are usually observed are shown as red dots, and the three that are used to inspect the cusp relations are the ones inside the small black circles. The blue square is the source position. The softening adopted for this lens map is 0.5 Kpc.

5.2 Cusp caustic relation

There are basically three configurations of four-image systems: fold, cusp and cross. In this paper, we will mainly concentrate on the *cusp* configuration that corresponds to a source located close to the cusp of the inner caustic curve. The behaviour of the gravitational lens mapping near a cusp was first studied by Blandford & Narayan (1986), Schneider & Weiss (1992), Mao (1992) and Zakharov (1995), who investigated the magnification properties of the cusp images, and concluded that the sum of the signed magnification factors of the three merging images approaches zero as the source moves towards the cusp. In other words (e.g. Zakharov 1995),

$$R_{\text{cusp}} = \frac{\mu_A + \mu_B + \mu_C}{|\mu_A| + |\mu_B| + |\mu_C|} \to 0, \quad \text{for} \quad \mu_{\text{tot}} \to \infty, \qquad (8)$$

where μ_{tot} is the unsigned sum of magnifications of all four images, and A, B and C are the triplet of images forming the smallest opening angle. By opening angle, we mean the angle measured from the galaxy centre and being spanned by two images of equal parity. The third image lies inside such an angle. This relation is an asymptotic relation and holds when the source approaches the cusp from inside the inner astroid caustic.

Since we know the lens position and the source position, the procedure of finding the cusp images is straightforward; we have identified the triplet of images belonging to the smallest opening angle; we have seen that the cusp images are better identified using as opening angle measured from the fourth image and being spanned by two images of equal parity. We have used this method only to find the cusp images; instead for testing the cusp relation (see equation 9), we have used the opening angle as defined from the centre of the galaxy ($\Delta\theta$).

Approximately 25 000 lens systems are generated with the source position inside the astroid caustic. Fig. 11 indicates in colour the value of R_{cusp} for all the different source positions; the apparent discontinuities originate from different image identifications. In the very centre of the caustic, the cusp relation is not well defined (what you have is mostly a 'cross relation', four images situated at the vertices of a cross centred on the cusp centre), as the source moves in the direction of the minor or major axes, we choose different subsets of three cusp images and therefore the discontinuity arises.
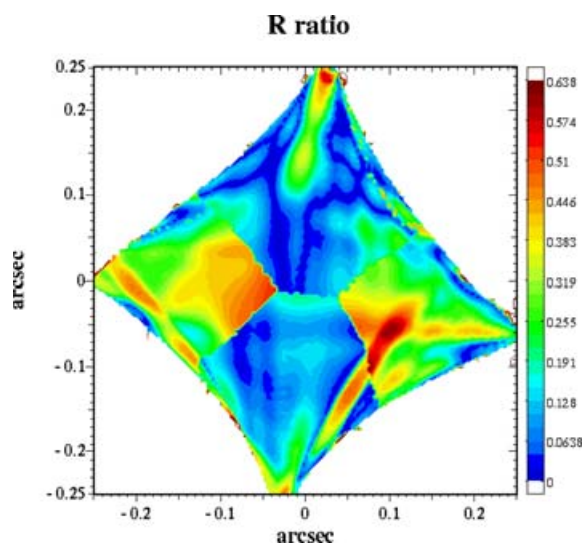
6 EFFECTS OF SUBSTRUCTURES

Because of the finite size (discreteness) of the particles in the simulations, there is a significant amount of shot noise in the surface density estimate, which can affect the lensing properties. The usual approach (Amara et al. 2004; Bradač et al. 2004) is to use a Gaussian kernel to smooth the surface density. In Amara et al. (2004), a detailed study of the impact and calibration of the smoothing was presented; their main conclusion was that a smoothing of 0.5 kpc is suitable for studying the cusp relation properties without losing any spatial information.

In order to try to disentangle the effects of bound substructures to the spurious effect produced by single finite particles, we have adopted a novel approach. We have tried to *remove* substructures from the lensing halo to see how this can change the cusp relation. Our removal procedure works as follows. First, we identified all bound substructures using SKID (see Section 3.2); then each particle belonging to any of the subhaloes is rotated around the centre of the galaxy using three random Euler angles. In order to avoid thin circular shells of particles, we added a random ±10 per cent error to each distance. We want to emphasize that we do not physically remove any substructures, because this will change the overall properties of the lens, mass, density profile, etc.

This procedure allows us to smooth out only the substructures leaving unaltered all the main features of the primary lens. In Fig. 12 (upper panel), we show the integral radial mass profile before and after the *removal* of the substructures; not only the total mass but also its radial profile is preserved. This means that all the lensing properties of the galaxy remain unchanged (critical curves, caustics and position of images) allowing us to make a one-to-one comparison between the two lensing maps. In Figs 13 and 14, the density map of the galaxy is shown, with and without substructures, respectively.

The cusp relation defined by equation (8) holds when the source is close to the cusp. As soon as the source moves away from the cusp, deviations from $R_{\text{cusp}} = 0$ are observed even for the smooth lens model. On the other hand, the closer the source is to the cusp, the smaller is the angle spanned from the three images. Therefore, in order to take into account the position of the source in evaluating
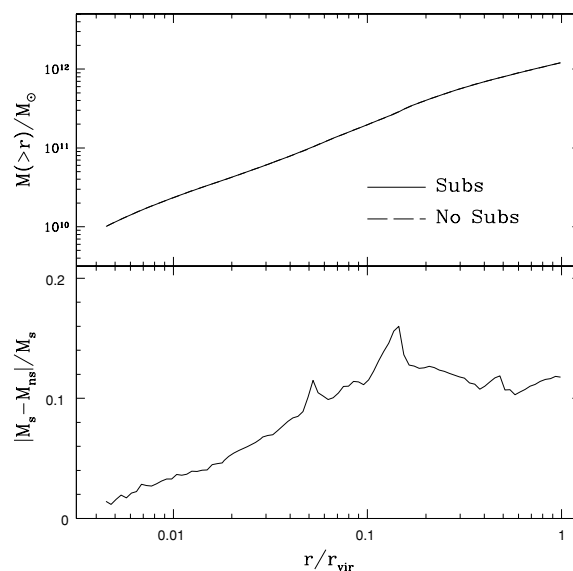

Figure 11. The value of the quantity R_{cusp} in the four-images region of the source plane; here a softening of 0.3 Kpc is used.

Figure 12. Mass versus radius before and after the removal of substructures. The overlap between the two curves is very good; in the lower panel, the residuals are shown.
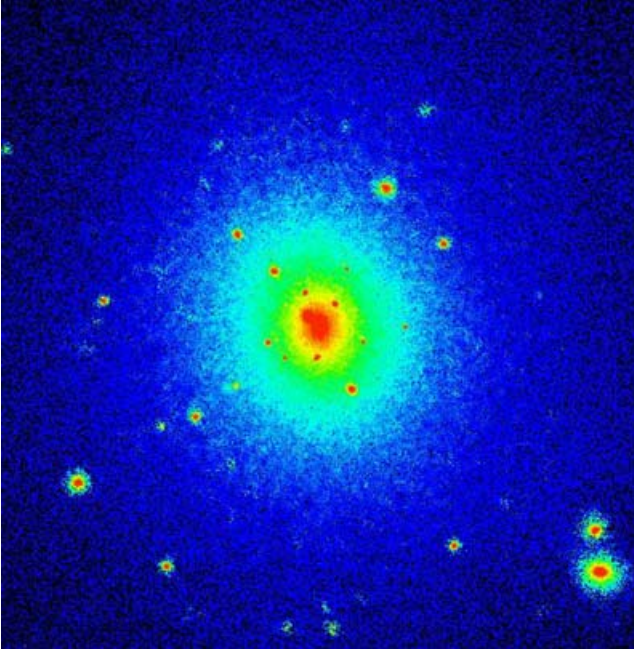
Figure 13. The density map of the mass distribution within the full hydrodynamical simulation. The size of the box is 200 kpc.
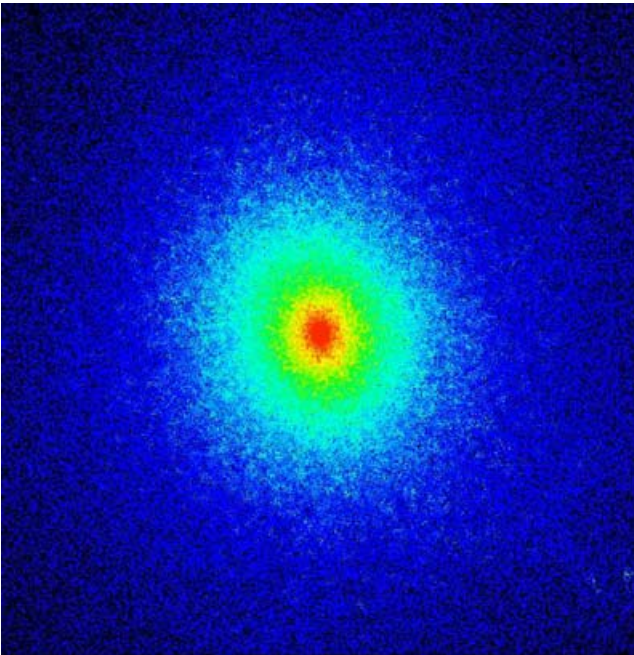

Figure 14. The density map of the smoothed mass distribution after randomizing the positions of the particles within the substructure haloes.

the cusp relation, it is better to define $R^0_{\rm cusp}$ as (see also Amara et al. 2004)

$$R^0_{\rm cusp} = \frac{2\pi}{\Delta\theta} R_{\rm cusp}, \tag{9}$$

where $\Delta\theta$ is the opening angle spanned by the two images with positive parity defined from the centre of the galaxy.

With this new definition of $R^0_{\rm cusp}$, a set of three images is said to violate the cusp relation if $R^0_{\rm cusp} > 1$. This makes the comparison between simulations and observations much more straightforward.

The differences in the reduced cusp relation violation in the two cases are shown in Fig. 16, where we plot the number of sources that violate the *reduced* cusp relation as a function of the Gaussian smoothing scale ($\epsilon_{\rm g}$). For both the lens models, the number of sources that violate equation (9) decreases with the smoothing length because the effect of smoothing is to reduce both the impact of substructures and the noise introduced by single particles.

The difference between the two is not so large, with a maximum of $\epsilon_{\rm g} = 0.5$ kpc, where the number of violations grows from 19 to 23 per cent; this is because this value of $\epsilon_{\rm g}$ is large enough to cancel the shot noise, but not large enough to smear out the subhaloes in the simulation, in good agreement with the results of Amara et al. For smaller value of $\epsilon_{\rm g}$, the signal is almost completely dominated by the shot noise, and for larger values we smooth too much, losing spatial information on the surface density of the lens.

Fig. 16 clearly shows that the impact of substructure in a mass range 10^7–10^9 is very weak in disturbing the cusp relation. The resolution achievable with current numerical simulations is still too poor to extend the analysis to a lower mass range of subhaloes; analytic arguments or semi-analytic prescriptions must be used (Macciò & Miranda 2005).

Nevertheless, a tentative comparison with observation can be made; there are five observed cusp caustic lens systems: B0712+472 (Jackson et al. 1998), B2045+265 (Koopmans et al. 2003), B1422+231 (Patnaik & Narasimha 2001), RXJ1131-1231 (Sluse et al. 2003) and RXJ0911+0551 (Keeton et al. 2003); the first three are observed in the radio band, the last two in optical and infrared (IR) band. Three of them violate the reduced cusp relation (i.e. $R_{\rm cusp} > \Delta\theta/2\pi$). This means a 60 per cent violation that is significantly larger than the 15–25 per cent we found for our simulations. The source size used in this work (60 pc) allows us to make a direct comparison mainly with the QSO observed in the radio band than in the optical or IR band; even in this case, we have a violation of the reduced cusp relation in two objects over three, that means 66 per cent violation. Fig. 15 shows the distribution of the values of the reduced cusp relation $R^0_{\rm cusp}$ both for data and simulates systems (with $\epsilon_{\rm g} = 0.5$ kpc). Simulation results are unable to reproduce the high-value tail that arises in the observational data; again it is
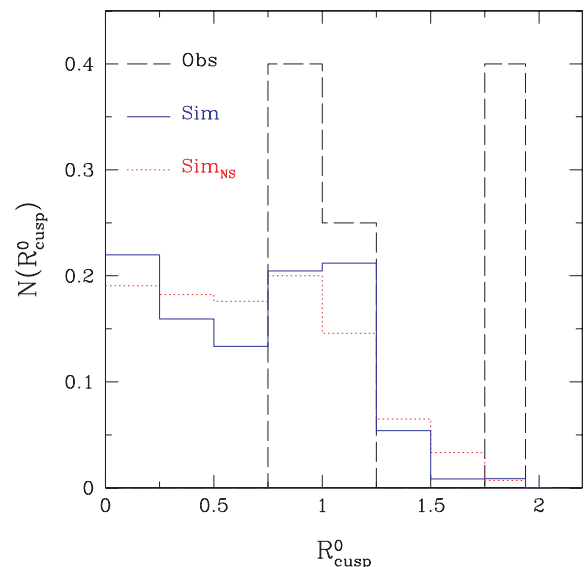

Figure 15. Distribution of $R^0_{\rm cusp}$ values. The solid and dotted lines show the simulation results before and after the substructure removal, respectively. The long dashed line represents the observational data.
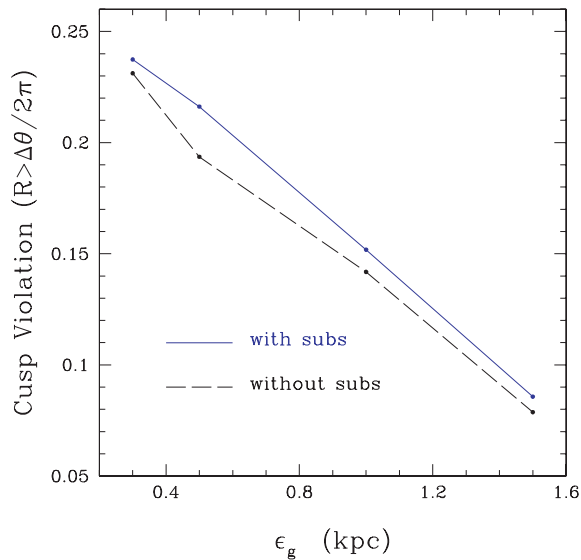
Figure 16. Fraction of total number of sources that violate the cusp relation as a function of the Gaussian smoothing length, ϵ_g. The solid line is for the whole galaxy and the dashed line is for the galaxy *without* substructures (see the text for its definition).

possible to see that the effect of subhaloes is very weak in disturbing the cusp relation, and they only marginally enhance the number of systems with $R_{\rm cusp}^0 > 1$.

As already discussed above, the difference between data and simulation results can arise from the current resolution limitations in the numerical simulations. We expect to have many more small DM haloes close to the centre of the galaxy with masses in the range 10^{-3}–$10^6\,M_\odot$; these haloes will be very concentrated, and so they can more easily survive the tidal force of the central halo, and if one of these haloes is close enough to one of the images, it can perturb its magnification and so violate the cusp relation. (The smaller is the mass of the subhalo, the closer it must be to the projected image position.)

Another possible explanation for the observed cusp relation violation can be ascribed to the effect of all the subhaloes that are in the galactic space along the line of sight of the lens (Metcalf 2005); the importance of these intergalactic haloes with mass $< 10^8\,M_\odot$ depends on the radial profile of the dark matter haloes and the primordial power spectrum at small scales.

What is clear from our analysis is that the cusp relation violation cannot be due to the substructures in the primary lens with masses above $10^7\,M_\odot$. This is true even though the inclusion of baryons has increased the projected numbers of subhaloes by a large factor.

7 DISCUSSION AND CONCLUSIONS

Using a high-resolution hydrodynamic galaxy formation simulation, we have studied the number density and the spatial distribution of subhaloes within a Milky Way sized CDM halo. Baryons can concentrate at the halo centre via two mechanisms. The shock-heated gas can radiate away energy causing the particles to fall inwards. Cold gas clouds can accrete along filaments, colliding and coalescing with existing gas at the halo centre. The slowly infalling baryons have the effect of increasing the density of the dark matter via adiabatic contraction. The overall effect of including baryons

is to steepen the mass profile to nearly isothermal with $\rho(r) \propto r^{-2}$ from a shallower r^{-1} cusp.

As already predicted by several (semi)analytic studies, our simulations show that this central concentration of baryons enables subhaloes to better withstand the tidal forces generated by the main halo. This leads to an increase in the total number of subhaloes, especially within the inner third of the virial radius, such that they follow the overall mass distribution. This is in excellent agreement with the distribution of galaxies within galaxy clusters. However, on the scale of Galactic mass haloes, this increases the discrepancy between the numbers of surviving satellites in the CDM models and the flat luminosity function observed within the Local Group. A possible solution to this problem may come from the early reionization of the universe from the early structure formation (Madau & Rees 2001). The reionization raises the entropy of the gas that is required to fuel galaxy formation, preventing it from accreting into small dark matter haloes and lengthening the cooling time of that gas which is accreted (Bullock, Kravtsov & Weinberg 2000; Ricotti, Gnedin & Shull 2002; Somerville 2002). Moreover, as suggested by Benson & Madau (2003), winds from pre-galactic starbursts and mini-quasars may pollute the intergalactic medium (IGM) with metals and raise its temperature to a much higher level than expected from the photoionization and so inhibit the formation of early galaxies.

A detailed study of the impact of the reionization on the formation of dwarf galaxies in hydrodynamic simulation will be presented in a forthcoming paper (Macciò et al. 2005b), where we show that with an appropriate choice of the reionization parameters and modelling, it is possible to reconcile observational data with the steep mass function of haloes and subhaloes within the CDM model.

In the second part of this work, we have explored the consequences of the increased number of satellites for multiply lensed quasar images by foreground galactic mass haloes, in particular the signatures on the violation of the so-called cusp relation. Previous work has reached different conclusions on this issue: Bradač et al. (2004) found an agreement between simulations and observations, but their results were limited by the low resolution of their simulations. Amara et al. (2004) (see also Mao et al. 2004) have shown that it is hard to reconcile the observed high number of cusp relation violation with results from simulations. Moreover, they have also shown that the shot noise due to the discreteness of the simulation (where every particle is in principle a substructure) plays an important role in changing the properties of the lens map. In order to disentangle the effect of substructures from the effect of having an intrinsic discrete distribution of matter, we compared results between haloes with and without any substructure present. We have developed a new technique to remove the satellites from the simulation without changing the overall matter distribution of the primary lens. This analysis demonstrates that the impact of subhaloes on lensing in the mass range 10^7–$10^{10}\,M_\odot$ is very small. Also, having a number of subhaloes which is about eight times higher than that of the observed one in this mass range, the number of multiple lensed QSO that shows a violation of the cusp relation (defined as in equation 9) is less than 24 per cent, in contrast with an observed one of about 60 per cent. Our results extend down to subhaloes of mass $10^7\,M_\odot$ due to the resolution limit of our simulations. Even considering the impact of smaller masses on subhaloes using an analytic approach does not help in solving the cusp relation problem (Macciò & Miranda 2005). A possible explanation could be that more variables must be taken into account in the lensing analysis, such as all the (sub)haloes that lie along the line of sight between us and the lens (see Chen et al. 2003; Metcalf 2005).

ACKNOWLEDGMENTS

REFERENCES

Amara A., Metcalf R. B., Cox T. J., Ostriker J. P., 2004, preprint (astro-ph/0411587)
Benson A. J., Madau P., 2003, MNRAS, 344, 835
Blandford R., Narayan R., 1986, ApJ, 310, 568
Blumenthal G. R., Faber S. M., Flores R., Primack J. R., 1986, ApJ, 301, 27
Bradač M., Schneider P., Lombardi M., Steinmetz M., Koopmans L. V. E., Navarro J. F., 2004, A&A, 423, 797
Bullock J. S., Kravtsov A. V., Weinberg D. H., 2000, ApJ, 539, 517
Chen J., Kravtsov A. V., Keeton C. R., 2003, ApJ, 592, 24
Chiba M., 2002, ApJ, 565, 17
Colin P., Klypin A. A., Kravtsov A. V., 2000, ApJ, 539, 561
Dalal N., Kochanek C. S., 2002, ApJ, 572, 25
De Lucia G., Kauffmann G., Springel V., White S. D. M., Lanzoni B., Stoehr F., Tormen G., Yoshida N., 2004, MNRAS, 348, 333
Diemand J., Moore B., Stadel J., 2004, MNRAS, 353, 624 (DMS04)
Gao L., De Lucia G., White S. D. M., Jenkins A., 2004a, MNRAS, 352, L1
Gao L., White S. D. M., Jenkins A., Stoehr F., Springel V., 2004b, MNRAS, 355, 819
Ghigna S., Moore B., Governato F., Lake G., Quinn T., Stadel J., 1998, MNRAS, 300, 146
Ghigna S., Moore B., Governato F., Lake G., Quinn T., Stadel J., 2000, ApJ, 544, 616
Gnedin O. Y., Kravtsov A. V., Klypin A. A., Nagai D., 2004, ApJ, 616, 16
Governato F. et al., 2004, ApJ, 607, 688
Haardt F., Madau P., 1996, ApJ, 461, 20
Hayashi E. et al., 2004, MNRAS, 355, 794
Jackson N. et al., 1998, MNRAS, 296, 483
Katz N., 1992, ApJ, 391, 502
Katz N., White S. D. M., 1993, ApJ, 412, 455
Keeton C. R., Gaudi B. S., Petters A. O., 2003, ApJ, 598, 138
Klypin A., Kravtsov A. V., Valenzuela O., Prada F., 1999, ApJ, 522, 82
Kochanek C. S., Dalal N., 2004, ApJ, 610, 69
Koopmans L. V. E. et al., 2003, ApJ, 595, 712
Kravtsov A. V., Gnedin O. Y., Klypin A. A., 2004, ApJ, 609, 482
Loeb A., Peebles P. J. E., 2003, ApJ, 589, 29
Macciò A. V., 2005, MNRAS, 361, 1250
Macciò A. V., Miranda M., 2005, preprint (astro-ph/0509598)
Madau P., Rees M. J., 2001, ApJ, 551, L27
Mao S., 1992, ApJ, 389, 63
Mao S., Schneider P., 1998, MNRAS, 295, 587
Mao S., Jing Y., Ostriker J. P., Weller J., 2004, ApJ, 604, L5
Mateo M. L., 1998, ARA&A, 36, 435
Metcalf R. B., Madau P., 2001, ApJ, 563, 9
Metcalf R. B., Zhao H., 2002, ApJ, 567, L5
Metcalf R. B., 2005, ApJ, 629, 673
Moore B., 2001, in Wheeler J. C., Martel H., eds, AIP Conf. Proc. Vol. 586. 20th Texas Symp. Relativistic Astrophysics. Am. Inst. Phys., New York, p. 73
Moore B., Katz N., Lake G., 1996, ApJ, 457, 455
Moore B., Governato F., Quinn T., Stadel J., Lake G., 1998, ApJ, 499, L5
Moore B., Ghigna S., Governato F., Lake G., Quinn T., Stadel J., Tozzi P., 1999, ApJ, 524, L19
Nagai D., Kravtsov A. V., 2005, ApJ, 618, 557
Navarro J. F., Frenk C. S., White S. D. M., 1996, ApJ, 462, 563
Patnaik A. R., Narasimha D., 2001, MNRAS, 326, 1403
Reed D., Governato F., Quinn T., Gardner J., Stadel J., Lake G., 2005, MNRAS, 380
Ricotti M., Gnedin N. Y., Shull J. M., 2002, ApJ, 575, 49
Schneider P., Weiss A., 1992, A&A, 260, 1
Sluse D. et al., 2003, A&A, 406, L43
Somerville R. S., 2002, ApJ, 572, L23
Stadel J., 2001, PhD thesis, Univ. Washington
Wadsley J. W., Stadel J., Quinn T., 2004, New Astron., 9, 137
Zakharov A. F., 1995, A&A, 293, 1
Zentner A. R., Kravtsov A. V., Gnedin O. Y., Klypin A. A., 2005a, ApJ, 629, 219
Zentner A. R., Berlind A. A., Bullock J. S., Kravtsov A. V., Wechsler R. H., 2005b, ApJ, 624, 505

This paper has been typeset from a TEX/LATEX file prepared by the author.